Chemical Science

EDGE ARTICLE

View Article Online
View Journal | View Issue

Cite this: *Chem. Sci.*, 2014, **5**, 1232

Scanning tunneling microscopy and small angle neutron scattering study of mixed monolayer protected gold nanoparticles in organic solvents†

Mauro Moglianetti,‡[a] Quy Khac Ong,‡[a] Javier Reguera,‡[a] Kellen M. Harkness,[a] Marta Mameli,[a] Aurel Radulescu,[b] Joachim Kohlbrecher,[c] Corinne Jud,[d] Dmitri I. Svergun*[e] and Francesco Stellacci*[a]

Received 16th September 2013
Accepted 13th November 2013

DOI: 10.1039/c3sc52595c

www.rsc.org/chemicalscience

When a binary mixture of ligand molecules is used to coat gold nanoparticles, stripe-like domains can occur. These nanodomains confer nanoparticles unique structure-dependent properties. The domain structure has been characterized primarily using scanning tunneling microscopy (STM) in air and in vacuum. Here we show the first STM images of striped nanoparticles in a solvent, 1-phenyloctane. We achieve stable imaging conditions on dodecanethiol–hexanethiol (C12 : C6) 2 : 1 protected gold nanoparticles. These features are persistent across many images and retain their direction and overall morphology when recorded at different scan angles. We also perform small angle neutron scattering (SANS) on two hybrid C6 : C12 nanoparticle samples dissolved in chloroform. The hybrid nanoparticles have the same composition and size distribution as samples imaged with STM, but one of the two ligands (either C6 or C12) is deuterated. Low resolution models reconstructed *ab initio* by simultaneous fitting of the SANS data reveal striped patterns of C6 and C12 on the gold surface. We use image analysis to quantitatively compare STM and SANS data, achieving remarkable agreement. This is the first paper to compare evidence of the existence of stripe-like domains for particles in solution using two independent techniques, and we believe that a combination of STM and SANS could become a major approach to characterize mixed ligand nanomaterials in solution.

Introduction

Self-assembled monolayers (SAMs) of thiolated ligand molecules on gold substrates are ordered two-dimensional crystals that spontaneously form upon immersion of a substrate in a solution containing the molecules. These molecules assemble through a dynamic process, and when a mixture of molecules is used, as long as there is a sufficient enthalpic driving force to lead to separation, domains spontaneously form.[1–3] Gold nanoparticles can be efficiently synthesized using SAMs as stabilizing agents. These SAMs constitute the ligand shell of the nanoparticles (NPs) and provide the NPs with a number of their interfacial properties. Separation on a flat Au surface and on the surface of Au NPs happens spontaneously in the ligand shell when SAMs are composed of a mixture of di-like ligand molecules.[4,5] Scanning tunneling microscopy (STM) studies in air have shown that this separation leads to the formation of stripe-like domains when binary mixtures of some ligands are used.[4–6] These domains in the ligand shell provide interesting properties to the particles, ranging from a structural component to interfacial energy, unique solubility behavior, cell membrane penetration, enhanced catalytic activity, and selective molecular recognition.[7–10] All of these properties occur with particles in a liquid.

The presence of stripe-like domains on the ligand shell of Au NPs has been identified through STM studies in air and in vacuum. These studies have established that the morphology and the width of these features are independent of the imaging parameters (mainly tip velocity).[5,6] In response to recent critiques of the interpretation of the STM images of striped nanoparticles,[11] studies have shown that these images can be reproduced effectively across laboratories, microscopes, and operators.[12] High-resolution images have been achieved allowing the characterization of the molecular arrangement within these domains.[13] Evidence of domains on NPs has also been established through FTIR, NMR, AFM, mass spectroscopy, and EPR studies.[9,14–17] The formation of these stripe-like domains is

[a]*Institute of Materials, École Polytechnique Fédérale de Lausanne (EPFL), 1015 Lausanne, Switzerland. E-mail: francesco.stellacci@epfl.ch*

[b]*Forschungszentrum Jülich GmbH, 52428 Jülich, Germany*

[c]*SINQ, Paul-Scherrer Institut, 5232 Villigen, Switzerland*

[d]*Adolphe Merkle Institute, University of Fribourg, 1723 Marly 1, Switzerland*

[e]*European Molecular Biology Laboratory, Hamburg Unit, EMBL c/o DESY, Notkestraße 85, Hamburg 22603, Germany. E-mail: Svergun@EMBL-Hamburg.de*

† Electronic supplementary information (ESI) available. See DOI: 10.1039/c3sc52595c

‡ These authors contributed equally to the paper.

due to a balance between the enthalpy of phase-separation between di-like molecules and the conformational interfacial entropy that takes place at the domain boundary between long and short molecules. This has been established using coarse grained and molecular dynamics simulations on NPs, as well as on nanorods.[18–21]

Despite extensive studies, the persistence of stripe-like domains against scan angle rotation has been tough to establish and indeed the prevalence of stripe-like domains perpendicular to the fast scan axis has been pointed out as a weakness in our images.[11] STM images in air and in vacuum have shown this rotation only a limited amount of times and for a small subset of the particles imaged.[5,22] Many are the reasons that have made the characterization of stripe-like domains against scan angle so hard. In order to establish the persistence of these domains against scan direction it is necessary to identify the exact same particles in images taken at different scan angles. This is challenging, given the intrinsic variability in stripe appearance and direction across nanoparticles. In addition, at room temperature there are known movements of ligand molecules on particles[23,24] and there may be movements of the tail-group of the molecules as a function of the interaction with the approaching tip. Both these phenomena will lead to small or large local variation in morphology of the stripe-like domains that ultimately lead to complex image interpretation. Finally, as one rotates the image, the tip approaches the sample from different directions; this in turn leads to a change in image resolution, due to variation in the convolution conditions and the asymmetry in tip shape. This can in part be mitigated using images that are the sum of the trace and retrace scan, but cannot avoid all of the issues related with the tip approaching the same particles from different angles.

Here we show, for the first time, that when particles are immersed in an apolar low-vapor pressure liquid (1-phenyloctane), the appearance of stripe-like domains becomes very consistent and stable across multiple images. This improvement leads to remarkable consistency in the stripe-like domains imaged at different scan angles for a good fraction of the nanoparticles imaged.

Small-angle neutron scattering (SANS) offers a unique opportunity to use contrast variation in order to study the nanoscale structures present at the surface of Au NPs thanks to the significant difference in neutron scattering contrast of hydrogen and deuterium. Contrast variation is achieved by selectively using deuterated and hydrogenous ligands. There are several reports in the literature[25–29] that describe the use of SANS techniques to characterize gold nanoparticles but the main focus of these studies was on the characterization of the dimensions of the gold core and of the thickness of the ligand shell. Von White *et al.*[28] provided a complete characterization of homoligand nanoparticles coated by either octadecanethiol (C18) or dodecanethiol (C12), addressing the effect of the solvent on the thickness of the ligand shell.

To the best of our knowledge, there are no reports of using SANS techniques to characterize the domain formation on the shell of thiolated nanoparticles. SANS has been used successfully to detect and characterize domains in multi-component lipid membranes of large vesicles.[30,31] A combination of contrast variation with specific deuteration in SANS is widely used to obtain low-resolution structures of proteins and complexes of biological macromolecules. Advanced computational methods are available to reconstruct three-dimensional models by simultaneous analysis of multiple SANS patterns,[32,33] and these methods were successfully applied to study objects such as ribosomes[34] and protein complexes.[35] In the present work, these methods are applied to analyze SANS data from coated nanoparticles with specifically deuterated ligands to visualize dodecanethiol and hexanethiol moieties on the surfaces of the gold particles. The SANS models display a remarkable agreement with the STM results and the joint use of the two methods appears as a highly effective tool to comprehensively characterize composite nanoparticles in solution.

Experimental

Materials and methods

Gold nanoparticles covered with mixtures of alkanethiols were synthesized using a modification of the method described by Zheng *et al.*[36] 0.25 mM chloro(triphenylphosphine)gold was dissolved in 20 mL of benzene and 0.5 mmol of ligands (0.33 mM of 1-dodecanethiol (C12) and 0.17 mM of 1-hexanethiol (C6)) was added and mixed for 10 min. After that, 2.5 mM of a borane *tert*-butylamine complex dissolved in 20 mL of benzene was added to reduce the sample. Once added, the solution was put immediately to reflux at 150 °C and left to react for one hour under strong stirring. The sample was precipitated with methanol and the purification was made in several cycles of centrifugation with methanol and acetone. ^{1}H NMR experiments performed in a Bruker 400 MHz were used to verify the cleanness of particles. The composition of the ligand shell was determined *via* ^{1}H NMR of the ligands after nanoparticle decomposition (Table S1 and Fig. S1†).

TEM images were taken in a Philips/FEI CM12 operating at 100 kV. The images were analyzed using the Image J software package [http://rsbweb.nih.gov/ij/]. The default threshold was used and the diameter was calculated with the area assuming the particles were spherical. The average core diameter of C12 : C6 2 : 1 NPs is 4.9 nm (Table S1 and Fig. S2†).

The particles were placed by the Langmuir–Schaefer technique on Au (111) on a mica substrate (Phasis, Switzerland) premodified with 1-butanethiol (C4) and hexadecanedithiol. A TEM grid was also covered using the same Langmuir–Schaefer technique used to prepare the STM samples. A representative image is shown in Fig. S3.†

STM images were acquired using a Bruker Multimode equipped with a Nanoscope IIIA using an E-scanner. STM tips were mechanically cut from Pt/Ir wires. A sample substrate was attached to a metal support disk using silver paint [http://www.2spi.com/]. Electrical connection from the sample surface to the base support was also made with silver paint. Before images were acquired, the scope system was allowed to run continuously for hours to equilibrate. It is particularly crucial to perform this step after 1-phenyloctane injection.

1-Phenyloctane (Sigma-Aldrich) was used without further purification.

The following range of image parameters were used: bias from 100–2000 mV, tunneling current setpoints from 50 pA to 2 nA, integral and proportional gains from 0.3–1, and tip velocity from 0.2–1.5 μm s^{-1}. Specific parameters for each image are noted in the figure captions. All images were acquired at 512 × 512 pixels. Image analysis was performed using Gwyddion open source software version 2.31 [http://gwyddion.net]. The first operation performed on all images was a second order background subtraction.

Power spectral density (PSD) is the norm squared of the Fourier transform of the STM topography images.[11] The horizontal PSD plots were obtained directly from the software. Sum and difference images were obtained using the software after 'Mutual Crop' of the trace and retrace images. Rotation of the images was obtained using the software with 'b-spline' interpolation. All of the topography images and the current images used in this edge article are shown in the ESI (Fig. S4–S8†).

SANS measurements were conducted on the KWS-2 beamline at the Jülich Center for Neutron Science at the FRM-II reactor, TU, Munich, Germany. Measurements were performed at room temperature, using 1.05 m sample-to-detector distance, at 5 Å wavelength with a collimation setup of 8 m. The samples were measured at a volume fraction of gold nanoparticles of 1.6×10^{-4}.

Results and discussion

Fig. 1 shows a representative image of the C12 : C6 NPs in 1-phenyloctane. Despite substantial attempts, we have not been able to convincingly image stripe-like domains on these particles in air. A representative image of this sample recorded in air is presented in Fig. S10.† Parts of the samples contained Janus particles,[37] but a significant portion of the sample had no identifiable structure on the particle ligand shell. The majority of particles were featureless. Prompted by this observation, we thought that it was plausible that in air the C12 molecules collapsed onto the much shorter C6 ones forming an almost homogeneous cover that made imaging features impossible. To address this problem and to remove the water condensate between the sample and the tip known to negatively affect imaging resolution, we decided to use 1-phenyloctane (a solvent for the C12 : C6 nanoparticles, as proven by UV-Vis measurements shown in Fig. S9†) to 'wet' the C12 and 'open-up' the particle surfaces. The results (shown in Fig. 1) were stunning, with clear stripe-like domains appearing in the images. Horizontal PSD analysis of the images shows that the characteristic spacing of these stripe-like domains is independent of tip speed (Fig. S11†). The PSD shown in Fig. 1d presents a shoulder in the region from ~1.6 nm ($k = 4$ nm^{-1}) to ~0.6 nm ($k = 10$ nm^{-1}) consistent with our recent findings on striped nanoparticles.[12] As a consequence we take the middle point (1.1 nm) as the characteristic width of the stripe-like domains on the particles. The Fourier transform of the image shown in Fig. 1a is shown in Fig. S12.†

Interestingly, when imaging in 1-phenyloctane (PO) we immediately observed a remarkable stability of the features in

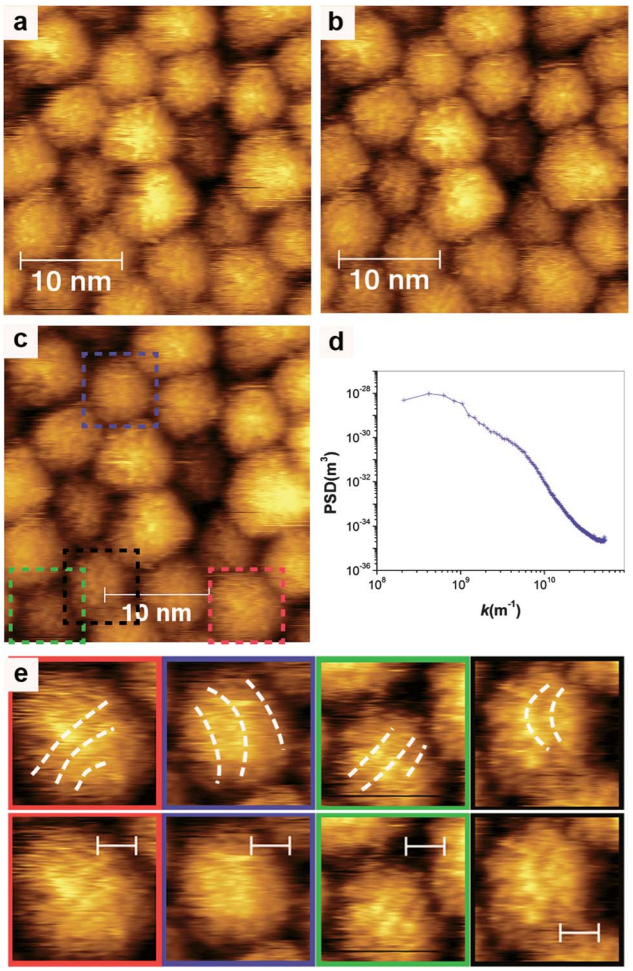

Fig. 1 STM topography images of the C12 : C6 sample. (a) Trace scan. (b) Retrace scan. (c) Sum image of the images a and b. (d) PSD spectrum of image (a). (e) Enlargements of parts of image (c), indicated with a colored box, each containing a particle showing stripe-like domains. Each particle is shown twice, as indicated by the color frame, the top image is meant as a guide to the eye to better visualize the bottom one. Dashed lines indicate the location and direction of stripe-like domains. Scale bars are 2 nm. Note that all of these images contain many horizontal streaks intrinsic to tip scanning. Bias V_b = 1500 mV, tunneling current I_t = 300 pA, scan length 30 nm, scan rate 20 Hz, tip velocity 1.22 μm s^{-1}, integral gain 0.43, proportional gain 0.9.

the STM images. This is probably because the PO molecules when wetting the C12 molecules provide them with a stable environment preventing substantial molecular movements during imaging. Additionally, the crispness of the images and their richness in detail may be due to PO dissolving, at least partially, some free ligands from the ligand shell of the particles. In air these free ligands would interact with the tip and blur images. Fig. 1a and b are the trace and retrace scans acquired as part of the same image. In Fig. 1c and S13† we show the sum and difference images between these two images. It is immediately evident that the difference image is almost featureless, showing significant differences only at the nanoparticle edges (where the direction of the tip-approach is very important). The sum image shows clearly the stripe-like domains with virtually no blurring of the features, indicating

the little movement happening for the ligand on the particles while imaging. Sum images also have the advantage of blurring the noise in the image; for these reasons hereafter we use them for image comparison. It should be pointed out that, while imaging, there is a certain amount of thermal drift of the sample relative to the tip position. This and the small offset that can be present between the trace and retrace scans of an image were corrected (in part) using the automatic feature "Mutual Crop" in Gwyddion.

Prompted by the remarkable stability in our imaging in PO we decided to test the persistence of our stripe-like features against scan angle. Fig. 2 shows five images taken as part of a sequence of images recorded at different scan angles. All images shown are the sum images of the trace and retrace scans. The single scans are shown in ESI, Fig. S4–S8.† In order to ease the comparison across different images, in Fig. 3 we re-show the same set of images shown in Fig. 2 digitally rotated according to the scan angle to display all of the particles and features in the same physical direction. It is evident, from a visual inspection of Fig. 2 and 3, that a large number of particles maintain the same morphology of the stripe-like domains across multiple images, with their direction clearly rotating according to scan angle. There are two characteristics of the images that we point out. First there is one particle, circled in red that keeps crisp stripe domains as a function of rotation. Second, there are rows of particles whose stripes are mostly aligned along the main axis of the row, as indicated by the white and green arrows at the left of these NP rows. As the row direction rotates so does the average directionality of the stripe.

The PSD plots shown in Fig. S14† basically overlap indicating a substantial consistency of the length scales of all of the features imaged. The white and green arrows in Fig. 2 and 3 indicate a certain average directionality in the stripe domains of the particles right close to them. In all of these images striped domains tend to have noticeable variability, with single particles showing domains that vary in direction and thickness in a single image. Yet, in the rows indicated there is a tendency of the main features of the domains to be mostly aligned with the direction indicated by the arrows, that is also the main axis of these particles' rows. We believe that the directionality present is probably due to some form of interdigitation between the ligands.[38] Indeed, the particle circled in green, that should have less defined interactions with surrounding NPs as it seems to lie below the others, has stripes roughly perpendicular to the arrows' direction (see Fig. S4, S5 and S8†). As a part of the row of particles that is indicated by the green arrow (Fig. 3), we notice a particle—marked with a white asterisk—that has a specific stripe morphology. It shows stripes aligned along the row main axis in the part of the particle pointing towards the red circled particle. In the other half of the particle, the images in Fig. 2d and e (and equivalently Fig. 3d and e) show a clear feature perpendicular to these stripes. This T-shaped motif rotates solidly when the scan angle is rotated 90°. This particle is a good example of the stable imaging condition that we achieved in PO as well as the complex patterns that can be imaged on this NP sample.

We can now focus on the particle that is highlighted using a red circle. This particle maintains its features across a large number of images and shows the same features when imaged again at zero scan angle seven images after the initial one. The persistence of the features is remarkable as is their crisp nature even when imaged at 90° from the original scan angle. It should be noted that this particle does not show equally crisp features in all images. In particular when imaged at a 30° scan angle the features become faint (but still identifiable when looking at line profiles). As the tip approaches the particles from different directions, the approach condition and the convolution effects

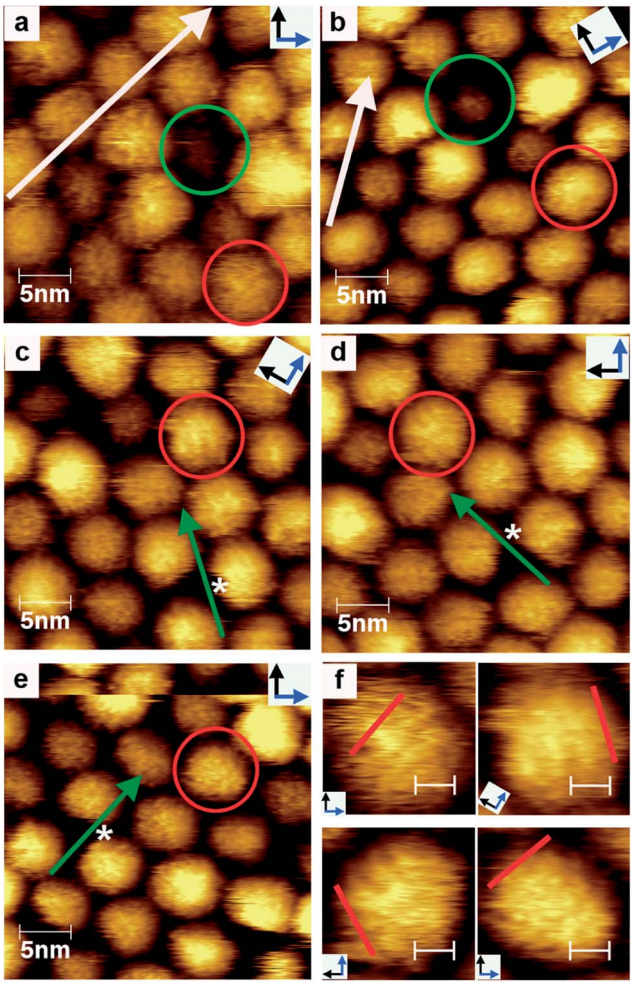

Fig. 2 STM topography images of the C12 : C6 sample acquired at different scanning angles. All images shown are the sum of the trace and retrace scan. They are shown in the same order they were acquired. (a) Scan angle (SA) = 0°. This is the same image shown in Fig. 1c. (b) 30°. (c) 60°. (d) 90°. (e) 0°. Large white and green arrows denote rows of particles sharing a general directionality in their stripe-like features (note the rows are made of the particles just to the right of the arrows, not below them). The red circles and white asterisks mark particles with clearly persistent stripe-like domains. Green circles mark an individual particle having stripes in a different direction from those nearby indicated by large arrows. All of these images were recorded with the same parameters described in the caption of Fig. 1. All images were recorded at 512 × 512 pixels; the images shown contain all those pixels with the exception of the few removed by the 'Mutual Crop'. (f) Enlargement of the particles marked by red circles in images (a), (c), (d), (e). Red straight lines serve to indicate the overall direction of stripes. Scale bars are 2 nm.

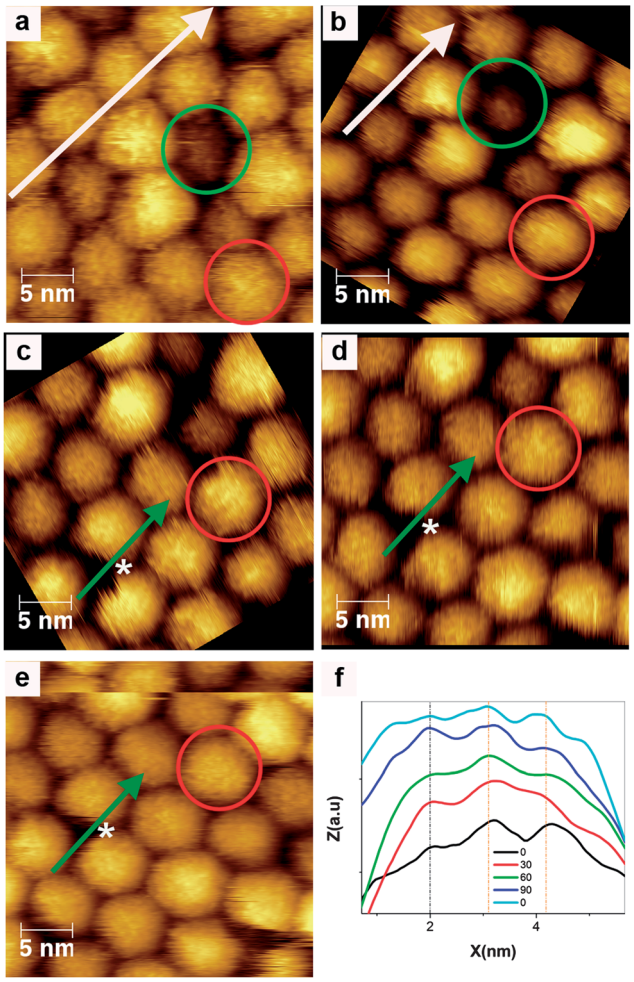

Fig. 3 Digital rotations of the STM images shown in Fig. 2. (a) Rotation angle (RA) = 0°. (b) −30°. (c) −60°. (d) −90°. (e) 0°. (f) Line profile analysis of the particle marked by red circles with legend numbers indicating the scan angles. The large white and green arrows are the same as shown in Fig. 2.

change as the tip does not have a symmetrical shape. Hence the specific and local conditions should not be expected to be exactly the same for all imaging directions. To better highlight the persistence of the stripes across images we undertook a profile analysis. We defined a line profile (30 pixels thick) in the direction we identified as roughly perpendicular to the stripes present in Fig. 3a. Using software features we maintained the same length and direction of the line profile and transferred it to the other four images shown in Fig. 3. We show in Fig. 3f the resulting five line profiles offset in height for clarity. The line profiles were aligned so that the first peak present would coincide (as indicated in the figure by a dashed black vertical line). The dashed orange lines are guides to the eye showing the remarkable persistence of the peaks in the line profiles. The inter-peak spacing that we find is 1.2 nm. We should point out that the images we are using were not drift corrected, hence each nanoparticle presents a distortion that obviously changes depending on the scan angle (and scan direction). The results shown in Fig. 3f have a remarkable consistency; we believe that the alignment of the peak substantially mitigates the drift effects. The exact line profiles used are shown in Fig. S8.†

To better investigate the structure of the ligand shell we complemented the STM studies with small angle neutron scattering (SANS) on diluted solutions of these particles in deuterated chloroform (see Experimental details in ESI†). Two different particles were synthesized alternately replacing the C6 and C12 ligands with their perdeuterated analogues. The synthetic methods were kept identical so as to obtain particles with the same size, size distribution, and ligand shell composition. Table S1 in the ESI† compares the size distribution data for the three particles used in this edge article (C6 : C12, d-C6 : C12, C6 : d-C12). Given the very small effect of deuteration on the assembly properties of molecules, one can safely assume that the three particles have similar ligand shell organization. In the conditions of the two SANS experiments, the deuterated ligand had positive contrast close to that of the gold, whereas the protonated ligand had a strong negative contrast (Table 1). The SANS data in Fig. 4a recorded for the two specifically deuterated particles displayed significant differences indicating that neutron scattering is sensitive to the deuteration of the ligands. The differences are even more pronounced in the distance distribution functions of the particles computed from the experimental data by Fourier transformation using GNOM[39] (Fig. 4b). Both hybrid particles have the same maximum size ($D_{max} = 75 \pm 5$ Å, *i.e.* diameter of the spherical search volume), and this observation agrees with the TEM data indicating that the particle size does not change upon specific deuteration (Table S1†). Note that the difference in size between the D_{max} and the TEM values has to be ascribed to the fact that SANS measurements provide the size of the whole particles, while TEM measures only the gold core size. The distance distributions as calculated from SANS data are drastically different for the two hybrid particles (Fig. 4b) yielding also significantly different radii of gyration (29.7 ± 0.5 Å for C6 : d-C12 and 34.2 ± 0.5 Å for d-C6 : C12), This difference reflects the contrast ratios of the two major components, gold and C12. For C6 : d-C12 particles, contrasts of gold and C12 moieties are positive and close to each other (Table 1) and the $p(r)$ function is bell shaped, which is typical for rather

Table 1 Contrasts of the phases in the hybrid particles (in units 10^{-6} Å^{-2}) (a) and discrepancy of the fits (b)

(a) Contrasts	C6 : d-C12	d-C6 : C12
Phase 1 : gold	1.4	1.4
Phase 2 : C12	2.5	−3.4
Phase 3 : C6	−3.4	1.9
(b) Discrepancy values[a]	C6 : d-C12	d-C6 : C12
Striped particle	1.2	1.1
Janus particle	15.2	7.7
Randomly mixed particles	1.8	4.2

[a] Chi squared.

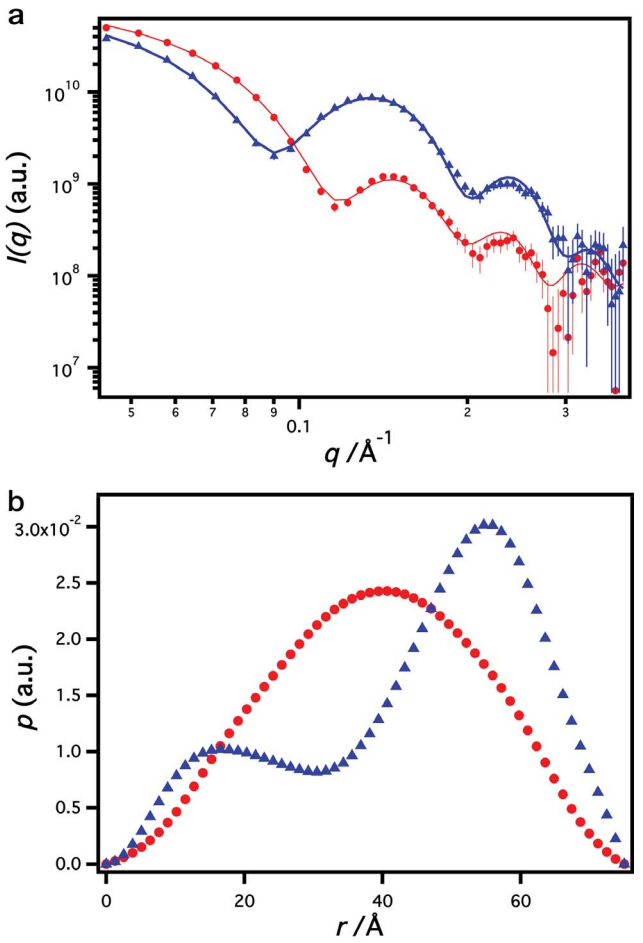

Fig. 4 (a) SANS data recorded for the C6 : d-C12 and d-C6 : C12 particles on diluted solutions in deuterated chloroform (C6 : d-C12 red circles, d-C6 : C12 blue triangles). Solid lines correspond to the fits calculated from the *ab initio* multiphase model whose result is depicted in Fig. 5 accounting for the appropriate contrasts of the gold, C6 and C12 moieties. (b) Distance distribution functions computed from the experimental data by indirect Fourier transformation using the program GNOM.

homogeneous globular bodies. For d-C6 : C12 particles, gold contrast stays positive and that of the C12 moiety is strongly negative (Table 1), leading to two peaks in the $p(r)$, the one for shorter interparticle distances corresponding largely to the gold core, the one for larger distances corresponding to the shell, dominated by protonated C12. Analysis of the model-independent overall parameters of the SANS data can therefore already provide insights into the spatial organization of the monolayer protected gold nanoparticles.

To obtain a more detailed low resolution model of the gold nanoparticles and the ligand shell from the SANS data, a multiphase version MONSA of the *ab initio* program DAMMIN[40] was employed. The program represents the entire particle as a collection of $M \gg 1$ densely packed beads of radius r_0 inside a spherical search volume with diameter D_{max}. To distinguish between the gold, C12 and C6 moieties the beads may have different contrast, which is related to the bead index. For this, each bead can be assigned either to the solvent (index = 0 and zero contrast) or to one of distinct components in the particle (index = 1, 2 and 3, corresponding to gold, C12 or C6 moieties). Given the fixed bead positions, which are defined by the packing grid, the structure of this dummy atom model (DAM) is described by a string of length $M \approx (D_{max}/2r_0)^3$ containing the phase index.

The modeling algorithm aims at simultaneous fitting of multiple data sets recorded in conditions where the phases have different contrasts. Given the contrasts, the scattering intensity from the given configuration of beads is rapidly obtained using a spherical harmonics expansion (see ESI†). Starting from a random string, simulated annealing (SA) is employed to search for a model composed by interconnected compact phases, which simultaneously fits multiple scattering curves from the constructs $I_k(q)$ to minimize overall discrepancy:

$$\chi^2 = \sum_k \frac{1}{N_k - 1} \sum_{j=1}^{N_k} \left[\frac{I_{exp}^{(k)}(q_j) - c_k I_{calc}^{(k)}(q_j)}{\sigma^{(k)}(q_j)} \right]^2$$

Here the index k runs over the scattering curves, N_k are the numbers of experimental points, c_k are scaling factors and $I_{calc}(q_j)$ and $\sigma(q_j)$ are the intensities calculated from the subsets of the beads belonging to the appropriate phases and the experimental errors at the momentum transfer q_j, respectively.

In the present case, two SANS patterns were available, from C6 : d-C12 and d-C6 : C12 particles, where the C6 and C12 moieties had opposite contrasts, as indicated in Table 1. The search volume of the model was a sphere of radius 38 Å, filled with over 4700 beads with the radius $r_0 = 2$ Å. To include the *a priori* information, beads with the radial distance from the center below 20 Å were fixed to be gold, those with the radial distance between 20 and 30 Å could belong to any of the three phases, and those with the radial distance exceeding 30 Å could belong to either C6 or C12. To test the hypothesis of having a Janus-type particle, the allowed bead assignments were modified in such a way that only beads belonging to a spherical cup of an appropriate volume could belong to a C6 moiety. To test the randomly mixed morphology, the beads representing C6 and C12 molecules were randomly generated in the shell in such a way that the total volumes of the C6 and C12 moieties were equal to those expected from the chemical composition of the composite particle.

The calculated patterns from the model at each SA step were appropriately smeared using the instrumental conditions of the KWS-2 beamline employing the analytical resolution function as introduced by Pedersen *et al.*[41] All MONSA calculations were repeated several times to verify and ensure reproducibility of the results.

Several MONSA runs starting from different random approximations were performed, yielding consistent and repeatable models and providing very good fits to the SANS data as illustrated in Fig. 4 (see the discrepancy values in Table 1). Fig. 5 displays a typical model with yellow beads indicating the gold regions, magenta beads the C6 regions, and cyan beads the C12 regions. One should note that the beads in the model are not meant to represent atoms and/or molecules; instead, they act as low resolution place holders

to depict the space occupied by the gold, C6 and C12 moieties. In the model, 1128 beads represent the gold nanoparticle, whereas the C6 and C12 moieties contain 390 and 2801 beads, respectively. The volume fractions of gold : C6 : C12 in the model are therefore 0.26 : 0.09 : 0.65, in excellent agreement with the volume ratio of the three components computed from the chemical composition (0.24 : 0.09 : 0.67). The centers of mass of all moieties are close (within 1 Å) from the origin. The gold moiety has R_g = 18.2 Å, those of C6 and C12 are 27.2 Å and 32.1 Å, respectively, indicating that, on average, C6 molecules occupy the space closer to the gold surface than the C12 molecules. The variation of the values of the overall parameters in different MONSA reconstructions was within 1–2% and the models had an overall appearance very similar to that in Fig. 5.[31,32,39] It is immediately evident that the model captures very well the facetted structure of the gold core, and also that the C6 regions form elongated domains within the bulk of the C12 phase, in excellent agreement with the model of striped nanoparticles. The arrows in Fig. 5 indicate domain boundaries (between C6 and C12) that the STM would image, and these boundaries are spaced at roughly 1 nm. To further verify that the SANS data are highly sensitive to the distribution of C6 and C12 in the shell, alternative models of ligand shell morphologies were also tried, specifically the Janus morphology as well as randomly mixed C6 and C12 molecules in the shell. The two models displayed in Fig. S15 and S16† had the same volume ratio of the components as the model in Fig. 5 and the same parameters of the gold core. For the random model, the radii of gyration of C6 and C12 moieties were practically identical (R_g = 31.8 and 32.2. Å) reflecting their random distribution in the shell surrounding the gold core. The Janus particle had a significant separation of 32 Å between the centers of mass of the C6 moiety (R_g = 21.5 Å) and C12 moiety, (R_g = 31.2. Å). For both random and Janus particles the best fits showed rather poor agreement with the experimental data (Fig. S15 and S16† and Table 1). In particular, the Janus morphology with a clear segregation between the C6 and C12 moieties, is not compatible with the SANS data. The reason is that pronounced maxima/minima in SANS patterns can only be observed for overall symmetric and close to concentric distributions. If one separates the phases asymmetrically, like in the Janus particle, the maxima/minima are significantly smeared. This effect is obvious in Fig. S15† leading to a dramatic worsening of the fits, as also evident from the discrepancies in Table 1.

The model presented in Fig. 5 shows elongated domains that have some degree of parallelism but has many C6 regions that run roughly perpendicular to these domains. Also, while most domains are right on the gold region, some seem to be far from it. One could be tempted to compare directly the model with the STM images, assuming that the STM will image mostly domain boundaries and miss in the images domains perpendicular to the main direction. The particle marked with an asterisk in Fig. 2 and 3 shows this very type of arrangement. This comparison might not be fully adequate, as the model derives from the fit of a polydisperse sample, with polydispersity in size and ligand shell morphology. To ensure a more reliable comparison we decided to use the model to produce an image close to the one we had in STM. We imported in a 3D rendering software the coordinate system from the model, used the C6 regions as the markers for the domain boundaries that we image in STM, replaced the gold region with spheres of equivalent size, and generated a layer of these particles randomly oriented (Fig. S17†). We then produced a grayscale image with the same number of particles acquired in the image shown in Fig. 1 and produced a PSD plot of this 'simulated' image in the same way used for STM images. As shown in Fig. 6 the PSD of the STM image and the one derived from the SANS data show the same features, indicating a quantitative agreement between the results in the two techniques. We do not believe that each feature in the PSD should be over-interpreted as the stripe like domains are complex but the agreement is certainly solid.

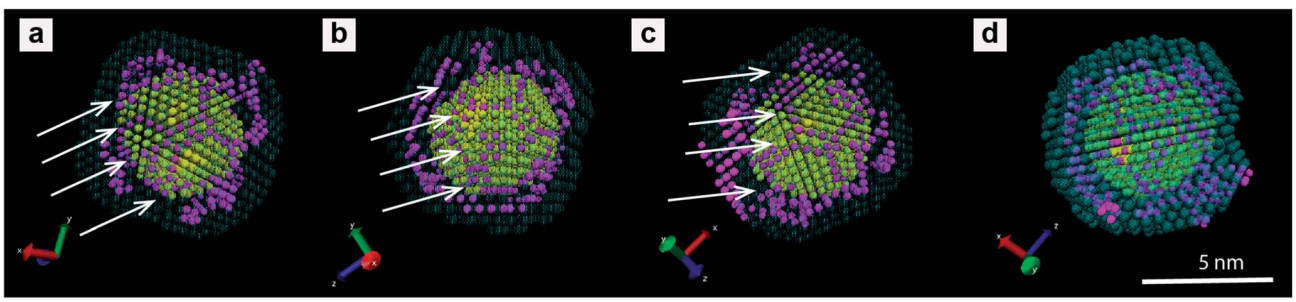

Fig. 5 Four different projections of a typical multiphase 3D low-resolution model of the C6 : C12 particles obtained from the fitting of the SANS data. Yellow beads indicate the gold nanoparticle core regions, the magenta beads represent the C6 moiety, and the cyan beads the C12 moiety. The beads in the model act as low-resolution place holders to depict the space occupied by the gold, C6 and C12 moieties. The image (d) on the right has the cyan beads in a lower transparency mode to highlight the C12 moieties. The C6 regions form elongated domains within the bulk of the C12 phase in excellent agreement with the model of striped nanoparticles. Scale bar, 5 nm. The arrows indicate elongated C6 domains that roughly align along a preferential direction. These features would provide aligned domain boundaries in the STM images (the arrows are spaced by about 1 nm).

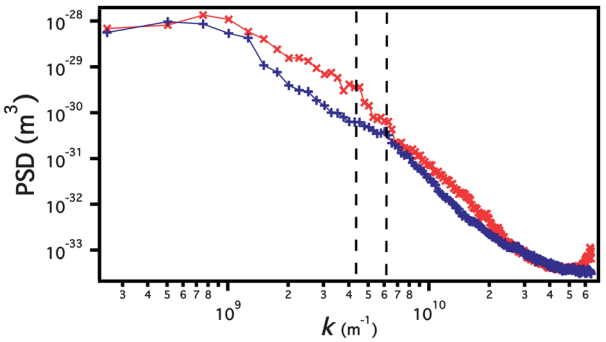

Fig. 6 PSD plots derived from the STM image (blue) shown in Fig. 1a and from the image simulated from the SANS data (red) shown in Fig. S17.† The PSD plots show evident similarities. In particular the dotted lines (4.3 and 6 nm^{-1} corresponding to 1.5 and 1 nm respectively) are at spatial frequencies where both plots present a small peak. For the STM derived plot these fall within the shoulder region (discussed in the text) that is due to the presence of stripe-like domains in the image.

Conclusions

In conclusion, here we have shown the presence of stripe-like domains for mixed ligand gold nanoparticles in organic solvents. STM images capture stripe-like domains on a few nanoparticles, whereas SANS averages over a large population. We show here that the two techniques converge to very similar models of the shell morphology. STM images acquired in PO show stripe-like domains that persist over a few images and maintain their direction against scanning angle rotation. SANS data on particles with alternatively deuterated ligands were simultaneously analyzed to provide a model, which also consistently displayed stripe-like domains. The SANS analysis procedure we used was initially developed for monodisperse systems, but it was demonstrated that these methods can be successfully employed for moderately polydisperse nanocomposites.[42,43] The qualitatively similar STM and SANS results were compared by creating a simulated image from the SANS derived model. The PSD of this image shows a remarkable quantitative agreement with the PSD of one STM image.

Acknowledgements

We are deeply grateful to Prof. Steven De Feyter and Dr Kunal Mali for the insightful discussion and the original suggestion of using liquids to improve STM imaging conditions. We thank Isabelle Grillo for the fruitful help and discussions about the best conditions for performing SANS of gold nanoparticles in liquids. We thank the Heinz Meier-Leibnitz Zentrum for the award of beam-time. We thank ILL for providing test time at D16 and D33. We thank Jan Ilavsky for fruitful help and discussion. We thank the Adolphe Merkle Institute (AMI) for allowing us to use its small angle X-ray scattering machine. K. M. H. gratefully acknowledges funding by the 7th Framework Programme of the European Commission (MCIIF 302989). M. M. gratefully acknowledges funding by the 7th Framework Programme of the European Commission (MCIEF 300928).

Notes and references

1 S. J. Stranick, S. V. Atre, A. N. Parikh, M. C. Wood, D. L. Allara, N. Winograd and P. S. Weiss, *Nanotechnology*, 1996, **7**, 438.
2 S. J. Stranick, A. N. Parikh, Y. T. Tao, D. L. Allara and P. S. Weiss, *J. Phys. Chem.*, 1994, **98**, 7636–7646.
3 S. J. Stranick, M. M. Kamna, K. R. Krom, A. N. Parikh, D. L. Allara and P. S. Weiss, *J. Vac. Sci. Technol., B*, 1994, **12**, 2004–2007.
4 A. M. Jackson, J. W. Myerson and F. Stellacci, *Nat. Mater.*, 2004, **3**, 330–336.
5 A. M. Jackson, Y. Hu, P. J. Silva and F. Stellacci, *J. Am. Chem. Soc.*, 2006, **128**, 11135–11149.
6 Y. Hu, B. H. Wunsch, S. Sahni and F. Stellacci, *J. Scanning Probe Microsc.*, 2009, **4**, 24–35.
7 A. Verma, O. Uzun, Y. H. Hu, Y. Hu, H. S. Han, N. Watson, S. L. Chen, D. J. Irvine and F. Stellacci, *Nat. Mater.*, 2008, **7**, 588–595.
8 A. Verma and F. Stellacci, *Small*, 2010, **6**, 12–21.
9 J. J. Kuna, K. Voitchovsky, C. Singh, H. Jiang, S. Mwenifumbo, P. K. Ghorai, M. M. Stevens, S. C. Glotzer and F. Stellacci, *Nat. Mater.*, 2009, **8**, 837–842.
10 A. Centrone, E. Penzo, M. Sharma, J. W. Myerson, A. M. Jackson, N. Marzari and F. Stellacci, *Proc. Natl. Acad. Sci. U. S. A.*, 2008, **105**, 9886–9891.
11 Y. Cesbron, C. P. Shaw, J. P. Birchall, P. Free and R. Lévy, *Small*, 2012, **8**, 3714–3719.
12 F. Biscarini, Q. K. Ong, C. Albonetti, F. Liscio, M. Longobardi, K. S. Mali, A. Ciesielski, J. Reguera, C. Renner, S. D. Feyter, P. Samorì and F. Stellacci, *Langmuir*, 2013, **29**, 13723–13734.
13 Q. K. Ong, J. Reguera, P. J. Silva, M. Moglianetti, K. Harkness, M. Longobardi, K. S. Mali, C. Renner, S. D. Feyter and F. Stellacci, *ACS Nano*, 2013, **7**, 8529–8539.
14 X. Liu, M. Yu, H. Kim, M. Mameli and F. Stellacci, *Nat. Commun.*, 2012, **3**, 1182–1190.
15 A. Centrone, Y. Hu, A. M. Jackson, G. Zerbi and F. Stellacci, *Small*, 2007, **3**, 814–817.
16 K. M. Harkness, A. Balinski, J. A. McLean and D. E. Cliffel, *Angew. Chem., Int. Ed.*, 2011, **50**, 10554–10559.
17 C. Gentilini, P. Franchi, E. Mileo, S. Polizzi, M. Lucarini and L. Pasquato, *Angew. Chem., Int. Ed.*, 2009, **48**, 3060–3064.
18 C. Singh, P. K. Ghorai, M. A. Horsch, A. M. Jackson, R. G. Larson, F. Stellacci and S. C. Glotzer, *Phys. Rev.Lett.*, 2007, **99**, 226106.
19 C. Singh, Y. Hu, B. P. Khanal, E. R. Zubarev, F. Stellacci and S. C. Glotzer, *Nanoscale*, 2011, **3**, 3244–3250.
20 W. L. Miller, B. Bozorgui, K. Klymko and A. Cacciuto, *J. Chem. Phys.*, 2011, **135**, 244902–244905.
21 S. A. Egorov, *Soft Matter*, 2012, **8**, 3971–3979.
22 M. Yu and F. Stellacci, *Small*, 2012, **8**, 3720–3726.
23 A. Caragheorgheopol and V. Chechik, *Phys. Chem. Chem. Phys.*, 2008, **10**, 5029–5041.
24 R. Hong, J. M. Fernandez, H. Nakade, R. Arvizo, T. Emrick and V. M. Rotello, *Chem. Commun.*, 2006, 2347–2349.

25 H. Jia, I. Grillo and S. Titmuss, *Langmuir*, 2010, **26**, 7482–7488.
26 M. Maccarini, G. Briganti, S. Rucareanu, X.-D. Lui, R. Sinibaldi, M. Sztucki and R. B. Lennox, *J. Phys. Chem. C*, 2010, **114**, 6937–6943.
27 K. Rahme, J. Oberdisse, R. Schweins, C. Gaillard, J.-D. Marty, C. Mingotaud and F. Gauffre, *ChemPhysChem*, 2008, **9**, 2230–2236.
28 G. Von White, F. S. Mohammed and C. L. Kitchens, *J. Phys. Chem. C*, 2011, **115**, 18397–18405.
29 M. Yoonessi, E. Seikel and M. J. Pender, *Langmuir*, 2009, **25**, 3369–3373.
30 V. N. P. Anghel, N. Kucerka, J. Pencer and J. Katsaras, *J. Appl. Crystallogr.*, 2007, **40**, 513–525.
31 J. Pencer, T. Mills, V. Anghel, S. Krueger, R. M. Epand and J. Katsaras, *Eur. Phys. J. E*, 2005, **18**, 447–458.
32 M. V. Petoukhov, D. Franke, A. V. Shkumatov, G. Tria, A. G. Kikhney, M. Gajda, C. Gorba, H. D. T. Mertens, P. V. Konarev and D. I. Svergun, *J. Appl. Crystallogr.*, 2012, **45**, 342–350.
33 M. V. Petoukhov and D. I. Svergun, *Int. J. Biochem. Cell Biol.*, 2013, **45**, 429–437.
34 D. I. Svergun and K. H. Nierhaus, *J. Biol. Chem.*, 2000, **275**, 14432–14439.
35 H. H. Niemann, M. V. Petoukhov, M. Härtlein, M. Moulin, E. Gherardi, P. Timmins, D. W. Heinz and D. I. Svergun, *J. Mol. Biol.*, 2008, **377**, 489–500.
36 N. Zheng, J. Fan and G. D. Stucky, *J. Am. Chem. Soc.*, 2006, **128**, 6550–6551.
37 J. Reguera, Q. Ong, I. C. Pons-Sieperman, M. Yu, S. C. Glotzer and F. Stellacci, 2013, submitted.
38 Z. L. Wang, *Adv. Mater.*, 1998, **10**, 13–30.
39 D. Svergun, *J. Appl. Crystallogr.*, 1992, **25**, 495–503.
40 D. I. Svergun, *Biophys. J.*, 1999, **76**, 2879–2886.
41 J. S. Pedersen, D. Posselt and K. Mortensen, *J. Appl. Crystallogr.*, 1990, **23**, 321–333.
42 E. V. Shtykova, A. Malyutin, J. Dyke, B. Stein, P. V. Konarev, B. Dragnea, D. I. Svergun and L. M. Bronstein, *J. Phys. Chem. C*, 2010, **114**, 21908–21913.
43 E. V. Shtykova, N. V. Kuchkina, Z. B. Shifrina, L. M. Bronstein and D. I. Svergun, *J. Phys. Chem. C*, 2012, **116**, 8069–8078.